A method to diagnose sources of annular mode timescales

Lawrence R. Mudryk[1] and Paul J. Kushner[1]

Received 4 November 2010; revised 4 April 2011; accepted 21 April 2011; published 28 July 2011.

Abstract. Timescales derived from Annular Mode (AM) variability provide dynamical insight into stratosphere-troposphere coupling and are linked to the strength of AM responses to climate forcings. AM timescales reflect decorrelation times of geopotential height in the stratosphere and troposphere. But geopotential height involves a vertical integral via the hypsometric equation, and this makes ambiguous some aspects of the dependence of the timescales on vertical level. In this study, a method for decomposing AM variability into contributions from surface pressure and from temperature is presented that is based on a linearization of the hypsometric equation. The decomposition is then used to interpret stratosphere-troposphere coupling events and the seasonal variation of AM timescales in reanalysis products and in two versions of a general circulation model that have distinctly different stratospheric representation. Surface pressure variations best account for tropospheric AM variability and stratospheric temperature variations best account for stratospheric AM variability during coupling events. But AM timescales are not so readily separated because they involve strong coupling between the surface pressure and stratospheric temperature variations: the pressure-temperature cross correlation functions are small in magnitude but highly persistent and thus provide significant sources of AM persistence. These empirical results provide a basis for further theoretical analysis on the origins of zonal mean stratosphere-troposphere coupling.

Citation: Mudryk, L. R. and P. J. Kushner (2011), A method to diagnose sources of annular mode time scales, *J. Geophys. Res., 116*, D14114, doi:10.1029/2010JD015291.

1. Introduction

The Northern and Southern Annular Modes (NAM, SAM) are the dominant pattern of variability in the extratropical circulation of each respective hemisphere [*Thompson and Wallace*, 1998, 2000]. During the active seasons of the stratosphere, the Annular Modes (AM) exhibit vertically coherent patterns extending from the surface to the stratosphere [*Thompson and Wallace*, 2000; *Baldwin and Dunkerton*, 1999]. This vertical coherence suggests coupling between the stratospheric and tropospheric circulation. This suggestion is further reinforced when we look at the time evolving behaviour of the AMs during the active season. NAM anomalies that originate in the mid- to upper stratosphere propagate downwards relatively slowly towards the lower stratosphere over 1-2 weeks. Once such anomalies reach the lower stratosphere, they rapidly descend throughout the entire troposphere [*Baldwin and Dunkerton*, 2001] (and Figure 4a, top). While the stratospheric AM is more persistent than the tropospheric AM for both radiative and dynamical reasons [*Charlton-Perez and O'Neill*, 2010; *Limpasuvan et al.*, 2005], the stratosphere-troposphere AM events described above give a qualitative impression that the relatively long timescale of persistence in the stratosphere can be temporarily transferred to the troposphere. Such an impression is reinforced by the seasonal evolution of the autocorrelation timescales for the AMs: the tropospheric AM is most persistent when the stratosphere itself is most persistent and active [*Baldwin et al.*, 2003] (and Figures 6a and 8a).

Despite the strong visual impression and diagnostic indications of AM coupling, the dynamics of such coupling remain poorly understood. A theory of this coupling would need to account for the distinctive dynamics of the stratospheric and tropospheric components of the AMs. In the stratosphere, AM variability reflects variations in the strength of the polar vortex that are strongly coupled to vertical fluxes of wave activity [eddy meridional heat fluxes, *Polvani and Waugh*, 2004; *Newman et al.*, 2001; *Hu and Tung*, 2002]. Tropospheric AM variability is more complex but can be most simply described as reflecting poleward and equatorward intensification of the jet that is coupled to meridional fluxes of wave activity [eddy momentum or vorticity fluxes, *Lorenz and Hartmann*, 2001, 2003]. These distinctive dynamics are captured separately by the *Holton and Mass* [1976] model of stratospheric polar vortex variability and the *Vallis et al.* [2004] barotropic model of tropospheric jet variability. But there is as yet no simple theory or simplified model that couples the two dynamics [*Kushner*, 2010]. Thus there is no simple theory for what sets the AM timescales.

Currently the most reduced mechanistic model for stratosphere-troposphere coupling is found in primitive equation general circulation models (GCMs) with simplified physics. With these models it is non-trivial to find stratosphere-troposphere coupling regimes [*Gerber and Polvani*, 2009] and the timescales of AM persistence in these models are highly non-robust [*Gerber et al.*, 2008b; *Chan and Plumb*, 2009]. For current comprehensive general circulation models, Gerber and others have used the autocorrelation timescale as a metric to test the realism of climate

[1]Department of Physics, University of Toronto, Toronto, Ontario, Canada.

Authors' Final Version
Journal version available from publisher

models [*Kidston and Gerber*, 2010; *Gerber et al.*, 2008a, b, 2010; *Shaw and Perlwitz*, 2010]. Typically, even comprehensive GCMs with relatively coarse resolution in the stratosphere capture some of the main observed features of AM timescale structure in the troposphere and stratosphere. But tropospheric AMs tend to be too persistent, and the seasonal peak in persistence in the troposphere too broad and delayed relative to observations. *Gerber et al.* [2010] further show that the peak in persistence is also delayed in the stratosphere in general circulation models with good stratospheric representation. Work on understanding these problems, which have implications for seasonal prediction and the circulation response to climate change, is ongoing.

In this study we present a diagnostic approach intended to describe more clearly the nature of AM stratosphere-troposphere coupling events and the related issue of AM timescales. We do not seek to prove a specific hypothesis about stratosphere-troposphere AM coupling, but instead make the point that our diagnostic picture of this coupling needs improvement before developing the theory further. In particular, we explore an elementary idea suggested by the simple mechanistic models of *Holton and Mass* [1976] and *Vallis et al.* [2004]. The Holton-Mass model in its simplest form is a prognostic model for the stratospheric zonal wind, which can be represented by stratospheric temperature. The Vallis *et al*. model is a prognostic model for the barotropic stream function, which can be represented by surface pressure. The mechanistic models suggest that these two fields are, to some extent, dynamically separate, but observations suggest that they couple under some conditions. With this viewpoint in mind, we present an elementary method for explicitly decomposing AM variability into contributions from surface pressure and from temperature fields, based on a linearization of the geopotential height integral. The decomposition helps to separate stratospheric and tropospheric AM variability when applied to AM stratosphere-troposphere coupling events (hinted at in *Siegmund* [2005]) and highlights the role of coupling between surface pressure and temperature signals in determining AM timescales. The use of surface pressure and temperature as proxies for stratospheric and tropospheric AM variability has the advantage that they are easily understood variables. This approach is complementary to that of *McDaniel and Black* [2005], who examine AM variability by reconstructing potential vorticity fields from dynamic variables. We propose that the decomposition presented here might serve as a starting point for future analysis, emphasizing for example the coherence of the different components of the Eliassen-Palm flux with the different terms in the decomposition.

In Section 2 we describe the data used, the geopotential height decomposition, and some technical aspects of the EOF methods used. In Section 3 we apply this decomposition to observed data and to output from two general circulation models that have distinctly different stratospheric representation. We examine AM stratosphere-troposphere coupling events and persistence timescales, discuss the connections between this decomposition and eddy mean-flow interactions, and attribute difference sources of persistence. Finally, in Section 4 we summarize our conclusions.

2. Methods

2.1. Observed Data and Model Output

We analyze extratropical circulation statistics for observational data from reanalysis products as well as general circulation model output. The observational data used is from the NCEP and ERA-40 reanalysis products [*Kalnay et al.*, 1996; *Uppala et al.*, 2005]. Northern Hemisphere results use daily averaged data from 1958–2007 for NCEP and from 1961–2001 for ERA-40. For Southern Hemisphere circulation statistics, we use data from the satellite era starting at 1979.

Observations are compared to output from two configurations of the Canadian Middle Atmosphere Model [CMAM, *Scinocca et al.*, 2008]; the simulations are described and analyzed by *Sigmond et al.* [2008]; *Shaw et al.* [2009]; *Shaw and Perlwitz* [2010]; *Sigmond and Scinocca* [2010]. The models are distinguished by their stratospheric representation. The first model, "CMAM HIGH", has 71 vertical levels with a lid at 0.0006 hPa (approximately 100 km). The second model, "CMAM LOWERED", has 41 levels with a lid at 10 hPa (approximately 16 km); CMAM LOWERED levels correspond to CMAM HIGH levels below 10 hPa. The models, which are otherwise configured to be as similar as possible, are designed to systematically test the effects of stratospheric representation on stratosphere-troposphere coupling in intraseasonal and climate variability. An important detail of both CMAM models is that parametrized gravity wave momentum is deposited in the uppermost model layer, thereby conserving momentum in the vertical direction This constraint results in a physically consistent momentum budget in both models, and a more realistic model climatology in the CMAM LOWERED model compared to one in which the momentum constraint is violated [*Shaw et al.*, 2009]. *Shaw and Perlwitz* [2010] have investigated AM variability and timescales in these simulations during Northern Hemisphere winter, and we wish to see what further insights can be gained from the applying the diagnostics developed here to them. We use the control integrations of *Sigmond et al.* [2008], which are run with climatological SSTs and time-independent radiative forcing. Forty years of output are available for this analysis.

2.2. Geopotential Height Decomposition

For a hydrostatically balanced dry ideal gas, geopotential height may be calculated as a function of time t, pressure p, and horizontal position $\boldsymbol{x}$, according to the hyposmetric equation

$$Z(\boldsymbol{x},p,t) = \frac{R}{g}\int_p^{p_s(\boldsymbol{x},t)} \frac{T(\boldsymbol{x},p',t)}{p'}dp', \tag{1}$$

where p_s is the pressure at the surface, R is the specific gas constant and g is the gravitational constant. We denote the functional dependence of geopotential height on the temperature and surface pressure fields with the notation $Z\{T,p_s\}$, and expand T and p_s in equation (1) into a climatological mean indicated by an overbar and an anomaly indicated with a δ,

$$p_s = \overline{p}_s + \delta p_s, \quad T = \overline{T} + \delta T,$$

we find

$$\begin{aligned}
\delta Z &= Z\{\overline{p}_s+\delta p_s, \overline{T}+\delta T\} - Z\{\overline{p}_s,\overline{T}\} \\
&= \frac{R}{g}\left[\int_p^{\overline{p}_s+\delta p_s}\frac{\overline{T}+\delta T}{p'}dp' - \int_p^{\overline{p}_s}\frac{\overline{T}}{p'}dp'\right] \\
&= \frac{R}{g}\left[\int_{\overline{p}_s}^{\overline{p}_s+\delta p_s}\frac{\overline{T}}{p'}dp' + \int_p^{\overline{p}_s}\frac{\delta T}{p'}dp' + \int_{\overline{p}_s}^{\overline{p}_s+\delta p_s}\frac{\delta T}{p'}dp'\right].
\end{aligned}$$

In this expression, δZ is nonlinear in the anomalies δT and δp_s. The climatological state in the above expression can be any climatology, but for concreteness, we suppose it to be a daily climatology of zonal mean quantities. Thus, the anomalies represent daily departures of the zonal mean from the climatological zonal mean state. We note that the first and third terms are independent of pressure level p and thus represent surface contributions. To leading order in the anomalies, we have

$$\delta Z \approx \delta Z_L \equiv \delta Z_T + \delta Z_{p_s} \tag{2}$$

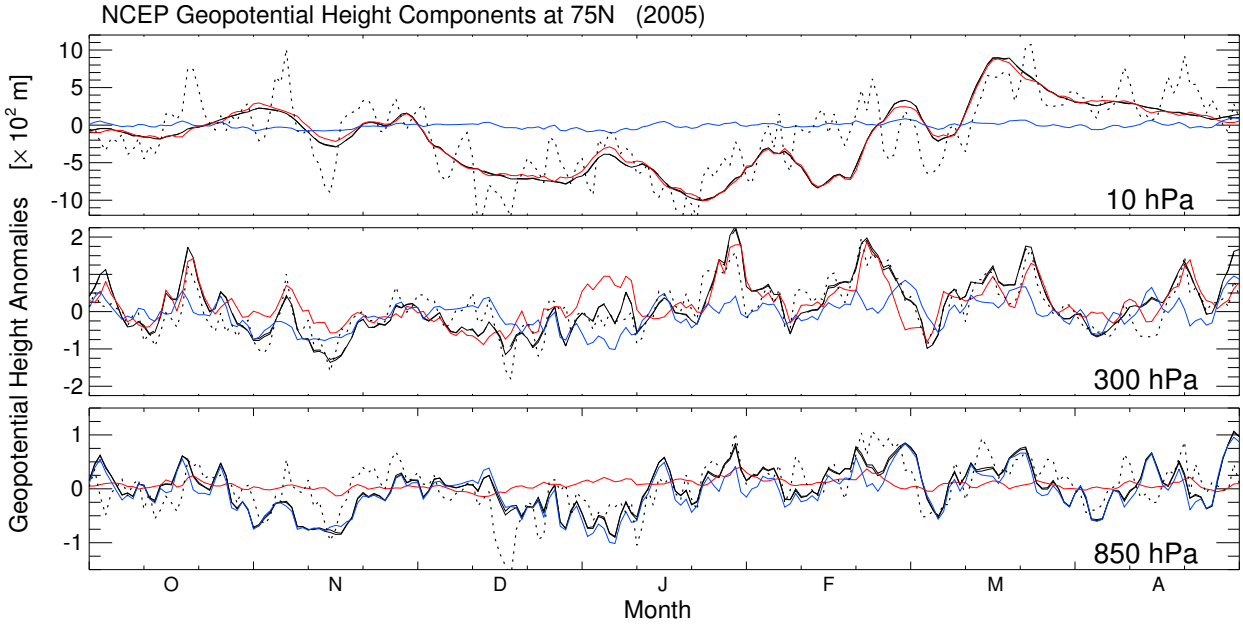

Figure 1. Solid black curves show the Northern Hemisphere zonal mean geopotential height anomaly δZ from the NCEP Reanalysis for 2005, relative to the 1958-2007 climatology, for (a) 10 hPa, (b) 300 hPa, and (c) 850 hPa. The black dashed curve shows $\delta Z - \delta Z_L$, where δZ_L is calculated from equations (2)–(4) using zonal mean temperature and surface pressure, multiplied by 100 in (a) and by 20 in (b)–(c). The solid red curve shows the temperature contribution δZ_T and the blue curve shows the surface pressure contribution δZ_{p_s}, which is independent of pressure level.

where δZ_L is the linearization of δZ; the contribution to δZ_L from temperature anomalies is

$$\delta Z_T(\boldsymbol{x},p,t) = \frac{R}{g}\int_p^{\overline{p}_s} \frac{\delta T}{p'}\,dp', \tag{3}$$

and the contribution to δZ_L from surface pressure anomalies is

$$\delta Z_{p_s}(\boldsymbol{x},t) = \frac{R}{g}\overline{T}(\boldsymbol{x},\overline{p}_s,t)\frac{\delta p_s}{\overline{p}_s}. \tag{4}$$

Thus, the linearization decomposes geopotential height anomalies into a pressure dependent term δZ_T that involves an integration over temperature anomalies and a pressure independent term δZ_{p_s} that is proportional to the fractional surface pressure variation. The higher order terms that are neglected in the linearization are second order in the amplitude of the anomalies, and include, among other terms, cross terms between the surface pressure and temperature. We expect this linearization to be accurate as long as the anomalies are relatively small compared to their climatological values and as long as the correlations between temperature and surface pressure remain small.

The example in Fig. 1 illustrates the contributions of the two components and the validity of the approximation. In this figure and the remainder of the study, we will use zonal mean fields for geopotential calculations. Thus we first calculate the zonal mean of δT and δp_s and input these into the calculation of δZ_L in equations (2)–(4), so that the result is also a zonal mean quantity. (Henceforth all δ anomalies refer to zonal mean quantities.) Fig. 1 compares the linearization δZ_L to the unapproximated zonal mean geopotential anomaly δZ, and includes the temperature contribution δZ_T and the surface pressure contribution δZ_{p_s}.

The key points of this example are that the linearization is accurate to within about 5%, with the agreement improving with altitude, and that the temperature contribution is dominant in the stratosphere (Fig. 1a), while the surface pressure contribution is dominant in the lower troposphere (Fig. 1c). In the upper troposphere (Fig. 1b) both contributions play a role.

The behavior illustrated in Fig. 1 holds more broadly, as illustrated in Fig. 2. The black curves in Fig. 2a represent the variance explained by the estimate. In particular, at each latitude, we calculate the temporal correlation of δZ and δZ_L and square the result; this represents the fraction of variance explained by the estimate at this latitude. The areal mean of the result over latitude, with cosine-of-latitude weighting, is calculated separately for each hemisphere and plotted as a function of pressure in Fig. 2a. Conclusions based on this and subsequent calculations in this section are insensitive to the cosine-of-latitude weighting and to whether the tropical latitudes are included or excluded. We aim here to be consistent with calculations of the Annular Modes by *Baldwin and Thompson* [2009], which also include the tropics. Note that the linear estimate accounts for almost all the variance in each hemisphere. The colored curves in Fig. 2a represent the relative role of the two terms in the linearization. In particular, equations (2)–(4) yield

$$\mathrm{var}(\delta Z_L) = \mathrm{var}(\delta Z_T) + 2\cdot\mathrm{cov}(\delta Z_T, \delta Z_{p_s}) + \mathrm{var}(\delta Z_{p_s}),$$

where "var" and "cov" indicate variance and covariance. We calculate these terms at each latitude and pressure level and plot in Fig. 2a the area-weighted mean (indicated with square brackets $[\cdot]$) of the following three quantities,

$$\left[\frac{\mathrm{var}(\delta Z_T)}{\mathrm{var}(\delta Z_L)}\right],\ \left[\frac{2\cdot\mathrm{cov}(\delta Z_T,\delta Z_{p_s})}{\mathrm{var}(\delta Z_L)}\right],\ \left[\frac{\mathrm{var}(\delta Z_{p_s})}{\mathrm{var}(\delta Z_L)}\right]$$

as a function of pressure level in red, green, and blue, respectively.

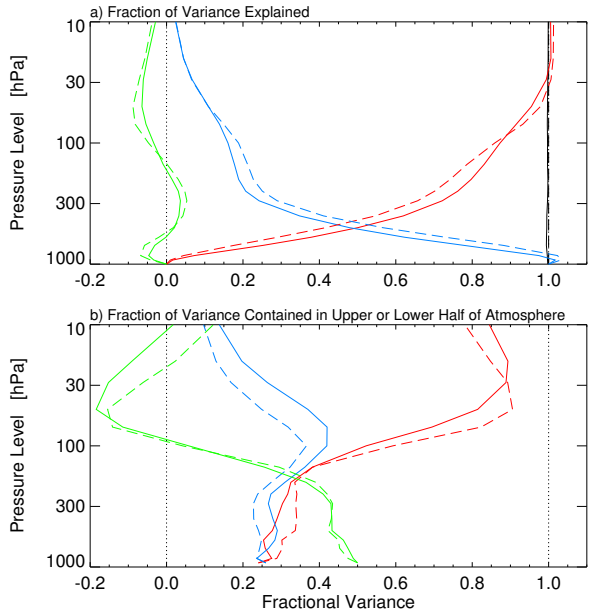

Figure 2. a) Correlation squared of δZ_L with δZ is plotted in black, the temperature term $[\mathrm{var}(\delta Z_T)/\mathrm{var}(\delta Z_L)]$ in red, the covariance term $[2\cdot\mathrm{cov}(\delta Z_T,\delta Z_{p_s})/\mathrm{var}(\delta Z_L)]$ in green, and the surface pressure term $[\mathrm{var}(\delta Z_{p_s})/\mathrm{var}(\delta Z_L)]$ in blue for Northern Hemisphere (solid) and Southern Hemisphere (dashed) NCEP Reanalysis data. b) The lower-level temperature integral term $[\mathrm{var}(\delta Z_{T,l})/\mathrm{var}(\delta Z_T)]$ is plotted in blue, the covariance term $[2\cdot\mathrm{cov}(\delta Z_{T,l},\delta Z_{T,u})/\mathrm{var}(\delta Z_T)]$ in green, and the upper-level temperature integral term $[\mathrm{var}(\delta Z_{T,u})/\mathrm{var}(\delta Z_T)]$ in red.

The surface pressure term δZ_{p_s} (blue curves) dominates below 400 hPa and the temperature term δZ_T (red curves) dominates above 300 hPa. The two terms are relatively decoupled: the covariance between the surface pressure and temperature contributions (green curves) is relatively small, representing typically less than 5% and at most 10% of the variance. We will return to the issue of the coupling of these terms in Section 3b.

We can show that the temperature term δZ_T in the stratosphere is most sensitive to stratospheric (local) temperature fluctuations, even though it is a vertical integral from the earth's surface.

From eqn. (3),

$$\delta Z_T = \delta Z_{T,l} + \delta Z_{T,u} \tag{5}$$

where the contributions to δZ_T from the lower-level and upper-level contributions to the integral, using log pressure as a variable of integration, are

$$\begin{aligned}\delta Z_{T,l} &\equiv \frac{R}{g}\int_{\frac{1}{2}(\ln p+\ln \overline{p}_s)}^{\ln \overline{p}_s} \delta T\, d\ln p', \quad \text{and}\\ \delta Z_{T,u} &\equiv \frac{R}{g}\int_{\ln p}^{\frac{1}{2}(\ln p+\ln \overline{p}_s)} \delta T\, d\ln p'.\end{aligned} \tag{6}$$

In Fig. 2b we plot the three terms

$$\left[\frac{\mathrm{var}(\delta Z_{T,u})}{\mathrm{var}(\delta Z_T)}\right],\ \left[\frac{2\cdot\mathrm{cov}(\delta Z_{T,l},\delta Z_{T,u})}{\mathrm{var}(\delta Z_T)}\right],\ \left[\frac{\mathrm{var}(\delta Z_{T,l})}{\mathrm{var}(\delta Z_T)}\right]$$

as a function of pressure level in red, green, and blue, respectively. In the troposphere, $\delta Z_{T,l}$ and $\delta Z_{T,u}$ contribute comparably and there is substantial covariance between the two. In fact, the fractional variances of the three terms listed above are approximately 0.25, 0.5 and 0.25, respectively, which are the values

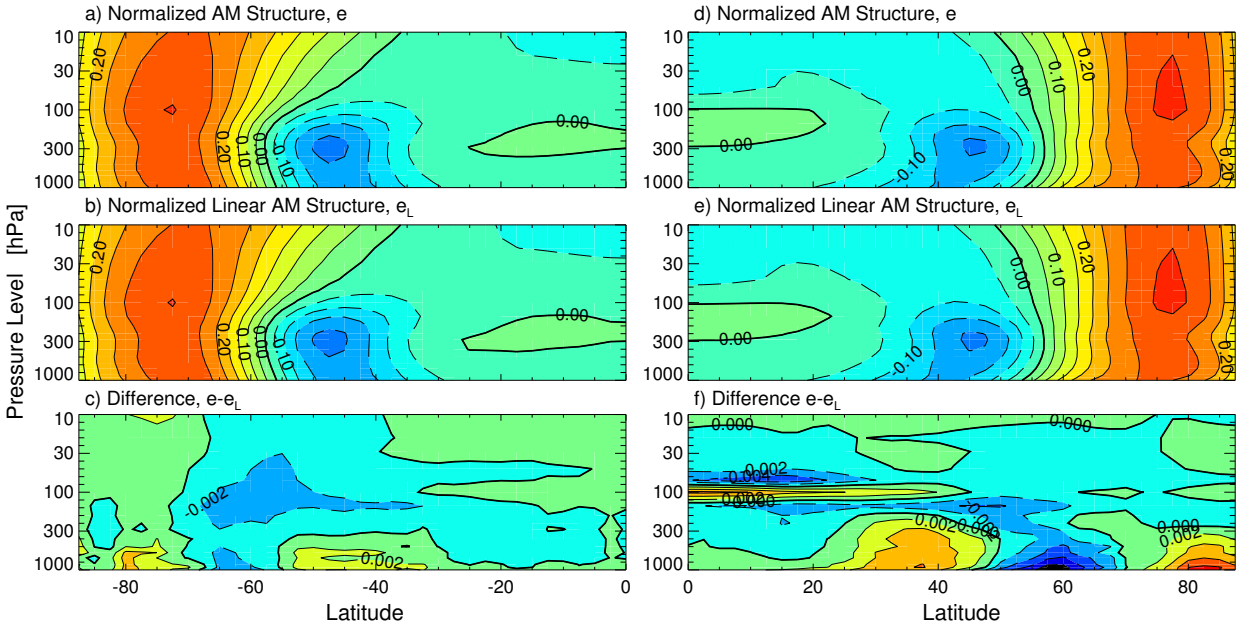

Figure 3. a,d) Meridional structure of the AM, $\boldsymbol{e}$, at each pressure level for the geopotential Z. The AMs are normalized to have the same meridional mean amplitude squared; b,e) As in panels a,d), for the AM, $\boldsymbol{e}_L$, based on the linear geopotential Z_L; c,f) Difference, $\boldsymbol{e}-\boldsymbol{e}_L$. Contour interval is 0.05 for the first two rows and 0.002 for last row.

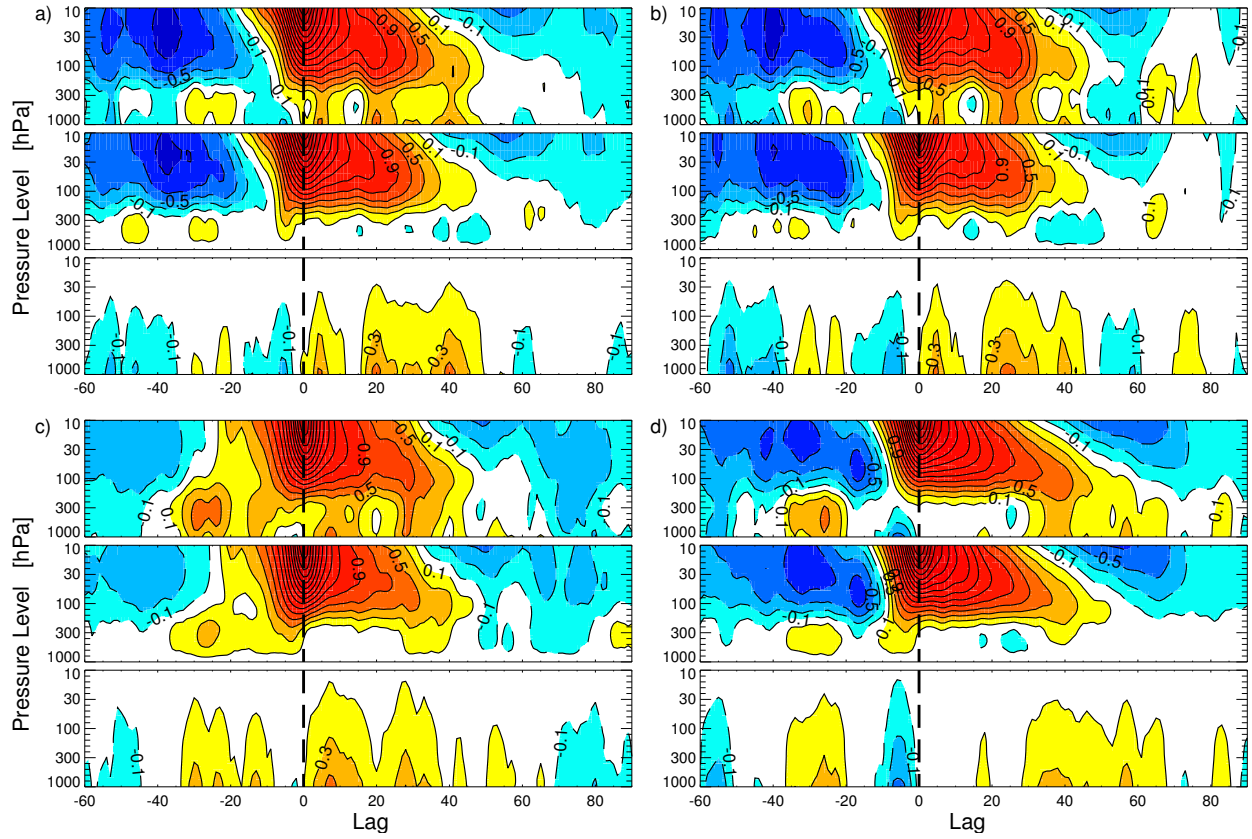

Figure 4. NAM composites of warm vortex events (1 per year). Plots show data from a) NCEP (50 years) b) ERA-40 (41 years) c) CMAM LOWERED (40 years) and d) CMAM HIGH (40 years). From top to bottom the panels show composites based on $\boldsymbol{y}_L$, $\boldsymbol{y}_T$ and $\boldsymbol{y}_{p_s}$, respectively. Contour intervals represent anomaly standard deviations and are spaced by 0.2. Index values between -0.1 and 0.1 are unshaded.

??

obtained for constant temperature anomalies, suggesting that the tropospheric parts of the curve may represent barotropic variability. On the other hand, above 100 hPa, when the lower boundary of the upper integration layer is above 300 hPa, the upper and lower contributions, $\delta Z_{T,l}$ and $\delta Z_{T,u}$ become uncoupled. This feature shows that it is stratospheric temperature fluctuations that account for stratospheric δZ_T fluctuations.

We summarize the main points arising from the decomposition: 1) the linearization of the geopotential represents an excellent approximation, 2) the surface pressure and temperature contributions are weakly coupled with the surface pressure term dominating in the lower troposphere and the temperature term dominating the upper troposphere and stratosphere, 3) the temperature contribution in the stratosphere reflects stratospheric temperature variability.

We define the SAM and NAM from δZ and δZ_L separately in each hemisphere. As calculated by *Baldwin and Thompson* [2009], the AMs are defined based on the zonal mean geopotential anomalies from daily data. The AM EOF pattern, denoted $\boldsymbol{e}$ along the lines of the notation of *Baldwin and Thompson* [2009], is the leading EOF at a given pressure level and in a given hemisphere. The principal component (PC) time series is extracted by the usual regression formula; for example, using the *Baldwin and Thompson* [2009] style of matrix notation, the PC time series for the AM for geopotential anomalies at each pressure level is

$$\boldsymbol{y} = \frac{\delta \boldsymbol{Z} \boldsymbol{W} \boldsymbol{e}}{\boldsymbol{e}^T \boldsymbol{W} \boldsymbol{e}}, \tag{7}$$

where $\delta \boldsymbol{Z}$ is the matrix form of the gridded geopotential field and $\boldsymbol{W}$ is a matrix which describes the spatial weighting applied to the original data set. The EOF $\boldsymbol{e}$ is dimensioned $[m \times 1]$, the weighting matrix $\boldsymbol{W}$ is dimensioned $[m \times m]$, and $\delta \boldsymbol{Z}$ is dimensioned $[n \times m]$, where n is the number of time points and m is the number of latitude points. All EOF calculations discussed in this paper are weighted by the horizontal area of the grid box. In this notation, using eqns. (2)–(4), we have the PC time series for the linearized geopotential at each pressure level and hemisphere:

$$\boldsymbol{y}_L = \frac{\delta \boldsymbol{Z}_L \boldsymbol{W} \boldsymbol{e}_L}{\boldsymbol{e}_L^T \boldsymbol{W} \boldsymbol{e}_L} \equiv \boldsymbol{y}_T + \boldsymbol{y}_{p_s}, \tag{8}$$

where $\boldsymbol{e}_L$ is the AM for the linearized geopotential,

$$\boldsymbol{y}_T = \frac{\delta \boldsymbol{Z}_T \boldsymbol{W} \boldsymbol{e}_L}{\boldsymbol{e}_L^T \boldsymbol{W} \boldsymbol{e}_L}, \text{ and } \boldsymbol{y}_{p_s} = \frac{\delta \boldsymbol{Z}_{p_s} \boldsymbol{W} \boldsymbol{e}_L}{\boldsymbol{e}_L^T \boldsymbol{W} \boldsymbol{e}_L}. \tag{9}$$

Note that the term $\boldsymbol{y}_{p_s}$ varies between pressure levels since the meridional structure of the AM $\boldsymbol{e}_L$ varies somewhat between pressure levels. However, the dependence of the AM's meridional structure on p is weak in the troposphere (see Fig. 3) implying that $\boldsymbol{y}_{p_s}$ variability is dominated by the p-independent term $\delta \boldsymbol{Z}_{p_s}$. Thus $\boldsymbol{y}_{p_s}$ is only weakly pressure dependent. For example, we find that the correlation between $\boldsymbol{y}_{p_s}$ at 1000 hPa and all levels with $p > 70$ is more than 0.99.

As expected from the similarity of δZ and its linear approximation δZ_L, the AMs based on δZ or on δZ_L are very similar.

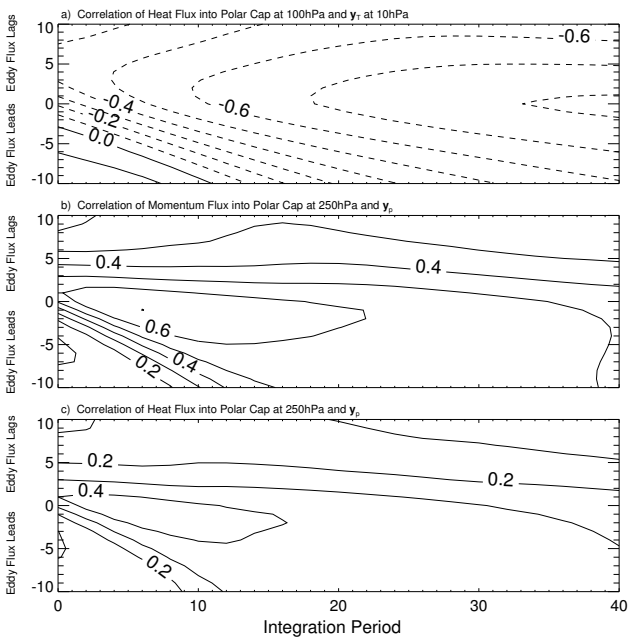

Figure 5. a) Correlation of wintertime (DJF) meridional eddy heat flux at 100 hPa (averaged from 45°N–75°N) with $\boldsymbol{y}_T$ at 10 hPa, which represents the NAM in the stratosphere, as a function of lag and integration period, from the NCEP Reanalysis. b–c) As in a), but for correlation of meridional momentum flux b) and heat flux c) at 250 hPa with $\boldsymbol{y}_{p_s}$, which represents the NAM in the lower troposphere. Fluxes are cumulative time averages over the period shown. The lag is the time from the end of the integration period to the time of the stratospheric or tropospheric component time series.

This is made clear in Fig. 3 which plots the normalized EOF structures, $\boldsymbol{e}$ and $\boldsymbol{e}_L$ and their difference, $\boldsymbol{e} - \boldsymbol{e}_L$ for both the the Northern and Southern Hemispheres. In both hemispheres, the differences are largest near the surface, consistent with the anomaly differences shown in Fig. 1. For the remainder of the paper we will present results using the linearized approximation only.

3. Results

The analysis in the preceeding section applies to anomalies of the geopotential height field in general. In this section we apply the decomposition and properties of the decomposition discussed there to an analysis of AM variability, including both stratosphere-troposphere coupling events and AM decorrelation timescales.

3.1. Decomposition of Stratosphere-Troposphere Coupling Events

Fig. 4 shows composites of weak vortex events [*Baldwin and Dunkerton*, 2001] for both NCEP and ERA-40 reanalysis products and the two 40-year CMAM integrations. We define a single weak vortex event for each winter season (NDJFM) as the day with the largest negative NAM index, based on the 10 hPa PC time series for the linearized geopotential $\boldsymbol{y}_L$. Composites of these selected events are shown in the top panels of each of the four plots. Results for the AM time series based on the nonlinear geopotential anomalies are very similar (not shown). The middle and bottom panels of each plot show composites of temperature component time series $\boldsymbol{y}_T$, and surface pressure component time series $\boldsymbol{y}_{p_s}$ for the same selection of warm events.

Fig. 4a shows the composites for NCEP data. Similar to the weak vortex composites shown by *Baldwin and Dunkerton* [2001], negative NAM anomalies originate above 10 hPa, propagate downward relatively slowly in the stratosphere, and then appear to descend rapidly through the troposphere. The second and third panels of Fig. 4a show that as for the geopotential anomalies themselves, the time series of the temperature component is the dominant a term determining the event composite in the stratosphere, while in the troposphere, the surface pressure time series is the dominate term determining the composite. That the surface pressure time series dominates the AM index even away from the surface up to about 300 hPa is the reason the downward phase propagation of NAM anomalies in the troposphere appears instantaneous. The surface pressure contribution is highly vertically coherent [see the discussion concerning eqn. (9)], and it is only in the upper troposphere and above that the integrated effect of the temperature anomalies via the $\boldsymbol{y}_T$ term begin to significantly alter the AM index — thereby destroying the vertical coherence. To further emphasize this point, we have redone these composite plots using a NAM index based on geopotential height averaged over the polar cap bounded by 60 degrees latitude (figures not shown). *Baldwin and Thompson* [2009] have shown that the polar cap geopotential is highly correlated with the NAM and so serves as an excellent proxy for the AM time series. We linearize the polar cap geopotential and decompose it into its surface pressure and temperature contributions, analogous to equations (2)–(4), and divide each contribution by the standard deviation of the linearized polar cap geopotential at each level. In this case, the surface pressure contribution is perfectly correlated at each level by construction, since all meridional dependence has been averaged out, and the temperature contribution is required to alter the vertical coherence of the NAM signals. Weak vortex composites based on this procedure lead to a near-replica of Figure 4 (not shown).

The tropospheric anomaly observed in the surface pressure component extends for a duration of 40–50 days which is roughly consistent with calculations of NAM timescales during DJF (see bottom panel of Fig. 6a). Results for strong vortex events (not shown) are similar to the weak events, with a somewhat slower rate of downward propagation observed for the pattern. We estimate the time of descent from 10 hPa to 100 hPa is about 7-8 days for weak vortex events and about a week longer for strong vortex events. This difference in evolution is consistent with results by *Limpasuvan et al.* [2005] who compare stratospheric sudden warmings with vortex intensification events. Results for ERA-40 (Fig. 4b) are very similar to NCEP. Turning to the analysis of the model output shown in Figs. 4c and 4d, the CMAM results appear realistic in the stratosphere (and hence in the temperature component of the height anomalies), but there are notable differences in the troposphere, as noted by *Shaw and Perlwitz* [2010], that can be attributed to contributions of the surface pressure to the composites. In particular, for the CMAM LOWERED model configuration, the pressure anomaly extends longer than observed, while for the CMAM HIGH model configuration, there is a large delay before the pressure anomaly appears. In addition, in both simulations there are positive AM signatures, arising both from warm temperature and positive surface pressure contributions, in the troposphere prior to the stratospheric event at day 0. While suggestions of such positive AM events seem to be present in the observations (Figs. 4a–b), they appear somewhat larger in the models (Figs. 4c–d).

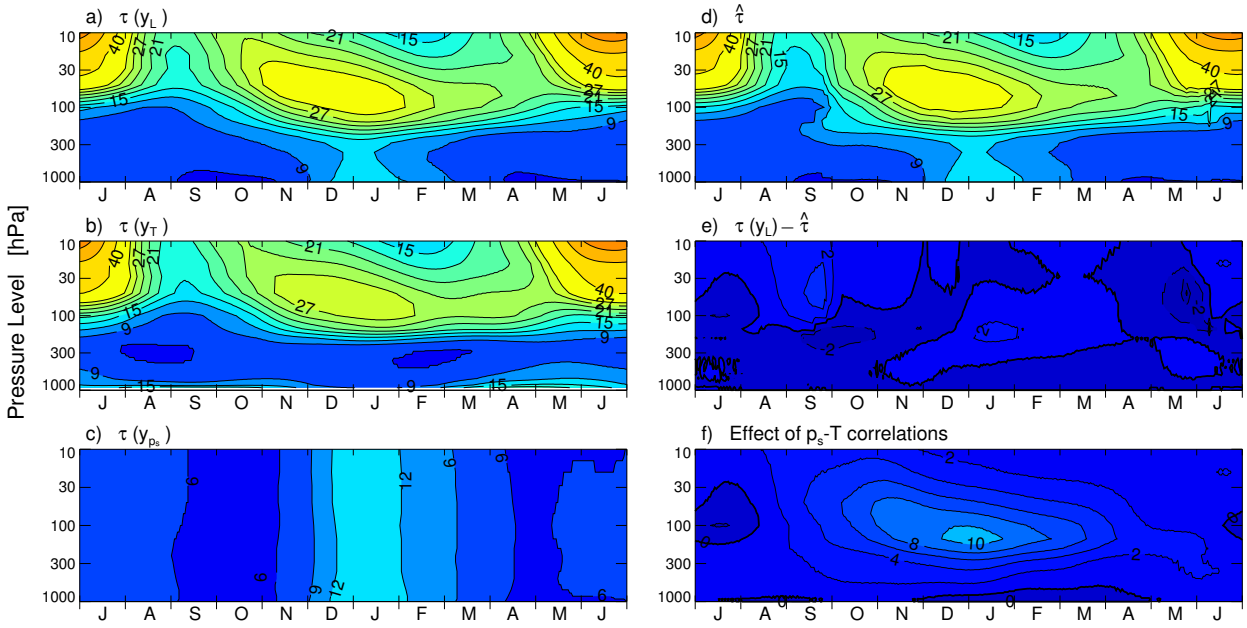

Figure 6. NAM timescale for the timeseries: a) $\boldsymbol{y}_L$, b) $\boldsymbol{y}_T$, c) $\boldsymbol{y}_{p_s}$ as a function of climatological month and pressure level, based on 50 years of NCEP data. We also plot d) effective timescale, $\hat{\tau}$ (see text), e) $\tau(\boldsymbol{y}_L) - \hat{\tau}$ and f) effect of $p_s - T$ correlations on $\hat{\tau}$ (see text).

The literature discussed in the introduction suggests that stratospheric and tropospheric AM variability are controlled by distinct contributions to the Eliassen Palm (EP) flux: stratospheric AM variability is primarily associated with variability in the vertical EP flux (eddy heat flux component), while tropospheric AM variability involves strong control by the horizontal EP flux (eddy momentum flux component) [*Hu and Tung*, 2002; *Lorenz and Hartmann*, 2001, 2003; *Newman et al.*, 2001; *Polvani and Waugh*, 2004; *Kushner*, 2010]. Specifically, the vertical component of the EP flux at 100 hPa is well correlated with the stratospheric NAM, when integrated over timescales near 40 days [*Polvani and Waugh*, 2004]. This behaviour is captured in Fig. 5a by the lag correlation of the average (cumulative) heat flux at various timescales with the temperature component of the NAM, $\boldsymbol{y}_T(10\,\text{hPa})$. As expected, the temperature component of the stratospheric NAM is only weakly correlated with the momentum flux (not shown). The horizontal component of the EP flux at 250 hPa is also well correlated with the tropospheric NAM over 1-2 week timescales. This behaviour is captured by the lag correlation of the average (cumulative) momentum flux with the surface pressure component $\boldsymbol{y}_{p_s}$ (Fig. 5b). The meridional eddy heat flux at 250 hPa displays a similar, though weaker, correlation structure with the tropospheric NAM, $\boldsymbol{y}_{p_s}$ (Fig. 5c). Because $\boldsymbol{y}_{p_s}$ explains the tropospheric component of the NAM, these correlations are consistent with the established picture of upward and equatorward propagation of baroclinic wave activity coherent with the NAM at high latitudes [*Limpasuvan and Hartmann*, 2000; *Lorenz and Hartmann*, 2003]. The Vallis et al. model, which represents vertical baroclinic wave activity fluxes as a flow-independent stochastic stirring, shows that NAM variability can be obtained only with coupling between the horizontal wave activity flux and the jet, and without explicit coupling between the vertical wave activity flux and the jet. But the situation in nature is more complex because the vertical component of the wave activity flux is significantly coupled to the jet as well, though more weakly than the horizontal component [*Lorenz and Hartmann*, 2003]; the importance of this coupling and its control on the NAM timescale is not known.

3.2. AM Timescales

Having examined the distinctive contribution of surface-pressure and temperature anomalies to stratosphere-troposphere coupling events like those shown in Fig. 4, we now turn to an analysis of the AM timescales. Fig. 6, which represents our principal result, shows the seasonal dependence of the timescale of the NAM for the NCEP Reanalysis and different ways of decomposing its sources. Figs. 6a-c plot the timescale τ for $\boldsymbol{y}_L$, $\boldsymbol{y}_T$ and $\boldsymbol{y}_{p_s}$ as a function of climatological month and pressure level, analogous to results shown by *Baldwin et al.* [2003]; *Gerber et al.* [2008a, b]; we denote these quantities $\tau(\boldsymbol{y}_L)$, $\tau(\boldsymbol{y}_T)$ and $\tau(\boldsymbol{y}_{p_s})$. The method used to calculate the timescale τ is based on code by E. P. Gerber and is documented in detail in the Appendix. Figs. 6d-f plot another set of timescale calculations which will be described below.

Fig. 6a shows the increased persistence of the NAM timescale during winter that *Baldwin et al.* [2003] attribute to stratosphere-troposphere coupling. Nearly identical results are obtained when we use the NAM time series $\boldsymbol{y}$, based on the nonlinear geopotential anomalies, instead of the linearization $\boldsymbol{y}_L$ (not shown). The timescales for the terms in the decomposition, $\tau(\boldsymbol{y}_T)$ and $\tau(\boldsymbol{y}_{p_s})$ provide diagnostic insight into the nature of this enhanced persistence. At first glance, the seasonal cycle of the NAM timescale $\tau(\boldsymbol{y}_L)$ in the stratosphere can be attributed to the stratospheric $\tau(\boldsymbol{y}_T)$, and the seasonal cycle of $\tau(\boldsymbol{y}_L)$ in the lower troposphere can be attributed to $\tau(\boldsymbol{y}_{p_s})$. But this attribution requires further analysis, because the timescales of the NAM are not simply additive in the timescales of the components. For example, the near surface $\tau(\boldsymbol{y}_T)$ is relatively long and is at a minimum in winter, which shows opposite seasonality to the NAM. Furthermore, the stratospheric $\tau(\boldsymbol{y}_{p_s})$ in DJF at 50 hPa is about 12 days, but $\tau(\boldsymbol{y}_T)$ is about 28 days in this period, which is only slightly shorter than the NAM timescale $\tau(y_L)$ there.

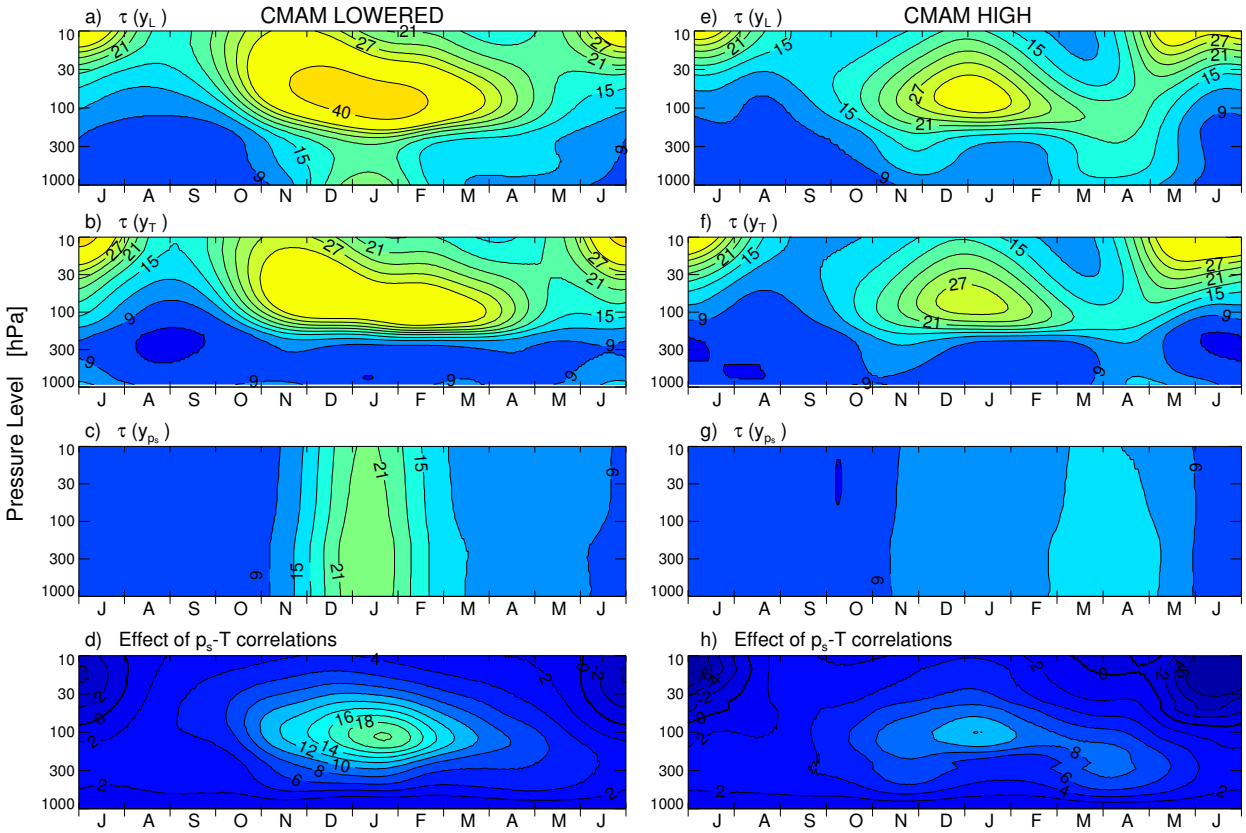

Figure 7. NAM timescales for CMAM LOWERED: a) $\tau(\boldsymbol{y}_L)$, b) $\tau(\boldsymbol{y}_T)$, c) $\tau(\boldsymbol{y}_{p_s})$ and d) effect of $p_s - T$ correlations on $\hat{\tau}$ (see text). Plots e–h are the same except for CMAM HIGH.

To more precisely attribute the timescales of the NAM to the surface-pressure and temperature contributions, we develop a timescale estimation procedure based on work by *Baldwin et al.* [2003] and *Gerber et al.* [2008a, b], which we extend to account for cross correlations between different contributions to the NAM timescale. As detailed in the appendix, the procedure involves estimating an effective timescale $\hat{\tau}$ for $\boldsymbol{y}_L$ that is consistent with the timescales of $\boldsymbol{y}_T$, $\boldsymbol{y}_{p_s}$ and their cross correlations. The seasonal and pressure dependence of this timescale is shown in Fig. 6d and the difference between this estimate and the original $\tau(y_L)$ is shown in Fig. 6e. The largest errors in the reconstruction result from fitting the the cross correlation timescale to an exponential when it is close to zero during stratospherically inactive seasons. The reconstructed timescale is able to capture the basic features of the original calculation, including the enhanced persistence in the troposphere and stratosphere in wintertime.

The calculation of the estimated timescale $\hat{\tau}$ is sensitive in an intriguing way to the cross correlations between $\boldsymbol{y}_T$ and $\boldsymbol{y}_{p_s}$. In the upper troposphere and lower stratosphere in winter, the terms $\boldsymbol{y}_T$ and $\boldsymbol{y}_{p_s}$ are weakly correlated but these correlations decay very slowly, on a timescale of about 100 days in DJF (see Fig. 10, which is described in the Appendix). Fig. 6f, which plots $\tau(\boldsymbol{y}_L)$ in Fig. 6a minus $\hat{\tau}$ calculated with the cross correlations set to zero (see Appendix), shows the impact of the cross correlations (we use $\tau(\boldsymbol{y}_L)$ when calculating this difference in order to minimize the error associated with fitting the cross correlation timescale to an exponential). The cross correlations are associated with enhanced persistence of the NAM, by as much as 10 days, in the lower stratosphere and upper troposphere from September to March. We have checked the robustness of these calculations for the ERA-40 dataset and find very similar results (not shown).

In summary, we find that the enhanced NAM timescale in the stratosphere is linked to local stratospheric temperature variations and in the troposphere is linked to local surface pressure fluctuations, but that in the lower stratosphere and upper troposphere much of the persistence is enhanced by fairly weak but highly persistent cross correlations between these quantities.

Repeating the NAM timescale calculations for the CMAM suggests where sources of bias might lie in these models. For CMAM LOWERED (Fig. 7a), unrealistically long persistence timescales are found in winter in the NAM timescale (as documented by *Shaw and Perlwitz* [2010]); these are associated with long timescales in surface pressure (Fig. 7c) and especially in the cross correlations (compare Fig. 7d with Fig. 6f). For CMAM HIGH (Fig. 7e), there is unrealistic enhanced persistence found in fall and spring and weak winter persistence in the troposphere [*Shaw and Perlwitz*, 2010]. These biases are associated with unrealistic tropospheric temperature persistence in fall (Fig. 7f) and, especially, unrealistic surface pressure persistence in spring and weak persistence in winter (Fig. 7g). By contrast, the model's stratosphere shows fairly realistic persistence in the fall and spring associated with realistic temperature persistence. The persistence timescales of the cross correlations are realistic in CMAM HIGH (Fig. 7h). *Shaw and Perlwitz* [2010] relate aspects of the persistence biases in these models to the character of wave reflection in them. Beyond this, the diagnostics developed here suggest a direction for further analysis of these differences; for example, the springtime surface pressure persistence

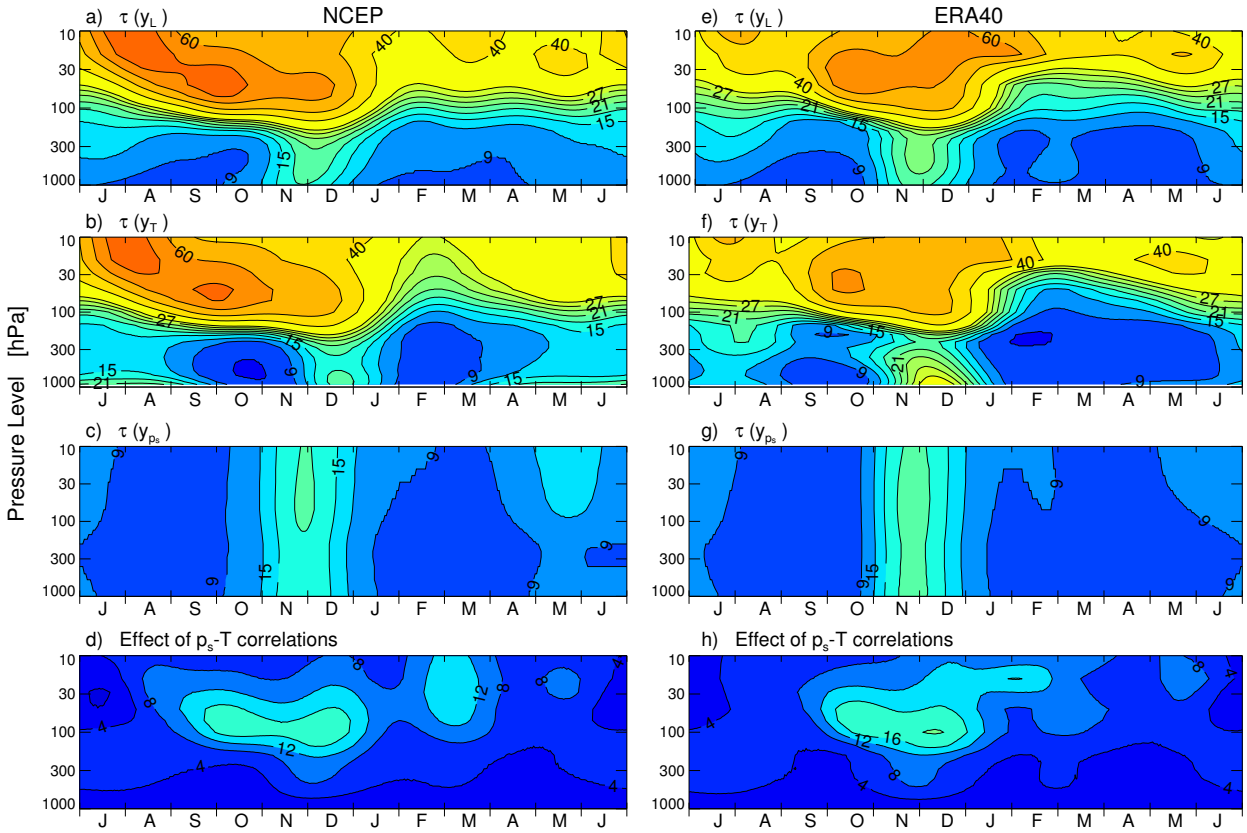

Figure 8. SAM timescales for NCEP data: a) $\tau(\boldsymbol{y}_L)$, b) $\tau(\boldsymbol{y}_T)$, c) $\tau(\boldsymbol{y}_{p_s})$ and d) effect of $p_s - T$ correlations on $\hat{\tau}$ (see text). Plots e–h show the same for ERA40 data.

bias might reflect a problem related to tropospheric variability, since the stratospheric and cross correlation timescales are reasonably well captured.

Fig. 8 shows the timescale decomposition for the SAM in the NCEP and ERA40 data. There are sizeable differences between the two products (although we have not determined the statistical significance of these differences), especially in their representation of the timescale of the temperature contribution $\boldsymbol{y}_T$. Unlike for the Northern Hemisphere, enhanced persistence in the troposphere is associated with contributions from both temperature fluctuations and surface pressure fluctuations. Akin to the model data for the Northern Hemisphere, CMAM data in the Southern Hemisphere shows unrealistically long persistence timescales starting from late winter and lasting throughout the spring (not shown, but documented by *Shaw and Perlwitz* [2010]). For both models, $\tau(\boldsymbol{y}_T)$ and $\tau(\boldsymbol{y}_{p_s})$ are unrealistically long and contribute to the unrealistic persistence (not shown). The models' cross correlation timescales contribute differently to the SH biases than the NH biases. The biases seen for the CMAM LOWERED model's cross correlation persistence in the NH are reduced in the SH (Fig. 9). The CMAM LOWERED model does indicate too much persistence due to cross correlations during DJF, however, there is less persistence associated with them in October as compared to the reanalysis products. By contrast, the persistence from the cross correlation terms in the CMAM HIGH model is too large throughout the winter, especially in November, as described for the temperature and surface pressure timescales of this model.

4. Conclusion

We have developed an empirical method for decomposing Annular Mode (AM) variability into contributions from surface pressure and temperature variations and have shown that timescales of AM variability can be quantitatively attributed to surface pressure variations, temperature variations, and the coupling between them. The decomposition is based on a linearization of the hypsometric equation that holds to excellent approximation (Figs. 1–3) and clarifies the separate contribution of stratospheric temperatures and surface pressures in stratosphere-troposphere coupling events. In these events, the surface pressure AM component dominates in the lower troposphere and the temperature AM component dominates in the upper troposphere and stratosphere (Fig. 4). The apparent rapid coupling between AM events from the lower stratosphere to the surface reflects the dominance of the surface pressure contributions relative to the temperature contributions to the geopotential anomalies. Furthermore, the temperature variability in the troposphere does not contribute strongly to the AM signatures of stratospheric events. Rather, the variability there is dominated by stratospheric temperature variations and as such reflects local variability (Fig. 2).

The empirical decomposition we present also helps to attribute distinct sources of persistence of the AM in the stratosphere and troposphere. The enhancement of the AM timescale during the active vortex seasons is primarily linked to persistent temperature variations in the stratosphere and to persistent surface pressure fluctuations in the troposphere. But to explain the enhanced persistence of the AMs in the lower stratosphere/upper troposphere, weak but highly persistent cross correlations between these quantities need to be considered (Figs. 6,10). These

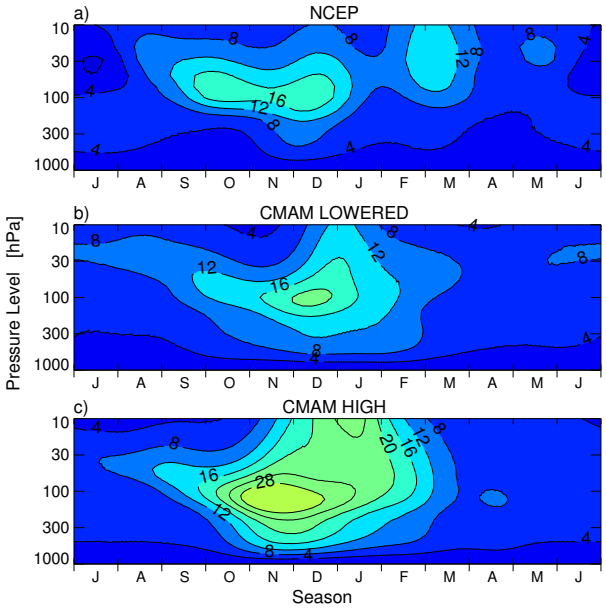

Figure 9. Effect of $p_s - T$ correlations in the Southern Hemisphere for a) NCEP (for comparison) b) CMAM LOWERED c) CMAM HIGH.

sources of persistence are represented distinctly in different models (Figs. 7,9) and are not always consistent in the two reanalysis products used here, especially in the Southern Hemisphere (Fig. 8).

Motivated by the *Holton and Mass* [1976] and *Vallis et al.* [2004] models of AM variability, our results suggest that surface pressure and stratospheric temperature are naturally separate dynamical variables that in the active seasons become weakly coupled in the upper troposphere/lower stratosphere. Our analysis quantifies the strength of that coupling during AM events and in AM timescales and highlights the control of different components of AM variability by different terms in the EP flux (Fig. 5). Furthermore, it shows that there might be different sources of AM timescale biases among climate models; these biases are in turn closely related to AM responses to climate change [e.g. *Kidston and Gerber*, 2010]. Based on the observed coupling between temperature and surface pressure in that region, we expect that cross correlations between zonal mean temperatures, surface pressure, and vertical and horizontal wave activity fluxes (eddy heat and momentum fluxes) will need to be accounted for in developing a theory for the AM timescales in the upper troposphere/lower stratosphere. The enhanced persistence in this region might represent an amplified feedback between zonal mean stratospheric flow and tropospheric synoptic eddy momentum fluxes, a coherence of the meridional and vertical EP fluxes for larger scale waves, or might reflect a direct driving of stratospheric wave fluxes on the surface pressure field [*Song and Robinson*, 2004; *Thompson et al.*, 2006]. Perhaps this theory will be best expressed from a potential vorticity (PV) viewpoint describing the time evolution of eddy PV fluxes and their coupling to the zonal mean PV field [*Robinson*, 2000]. Investigating these ideas will be the subject of future work.

Appendix A: Appendix

Based on the NAM timescale estimation procedures of *Baldwin et al.* [2003] and *Gerber et al.* [2008a, b] we proceed as follows: for each year n in an N-year dataset and for each (Julian) calendar day t_0, multiply a given time series $f(t)$ (such as the AM time series for linearized geopotential at pressure p, $\mathbf{y}_L(p,t)$) by a Gaussian mask with full width half maximum of 60 days that is centered on t_0. The filtered result is expressed as N segments centered on t_0; contributions from points where $|t-t_0| > 90$ days are neglected, and the time mean is removed. Denote the set of N segments that results as $\{f(n,t-t_0)\}$. Now consider two sets of times series so obtained, $\{f(n,t-t_0)\}$ and $\{g(n,t-t_0)\}$. We calculate their covariance with respect to the ensemble of years as $\langle f(n,t-t_0)g(n,t-t_0)\rangle$, where the angle brackets denote a time mean followed by a composite average across the n years. Extending this notation, the l-day lag cross-covariance between f and g for calendar day t_0 is $\mathrm{cov}(f,g;l) \equiv \langle f(n,t-t_0)g(n,t-t_0+l)\rangle$ [where g leads f by l days], the autocovariance $\sigma^2(f) \equiv \mathrm{cov}(f,f;l=0)$, and the lagged cross-correlation is $r(f,g;l) \equiv \mathrm{cov}(f,g;l)/\sqrt{\sigma^2(f)\sigma^2(g)}$.

The timescale estimate assumes a red noise autocorrelation model, whereby all correlations decay exponentially: i.e. $r(f,g;l) \approx r(f,g;0)\exp(-l/\tau(f,g))$, where $\tau(f,g)$ is the decay timescale for the cross correlation function. A least squares estimate is used to determine the value of $\tau(f,g)$ for each calendar day t_0 that minimizes the average over lag l, for $l \geq 0$, of the cost function

$$\sum_{l=0}^{l_{\max}} [\exp(-l/\tau(f,g)) - r(f,g;l)/r(f,g;l=0)]^2, \qquad \text{(A1)}$$

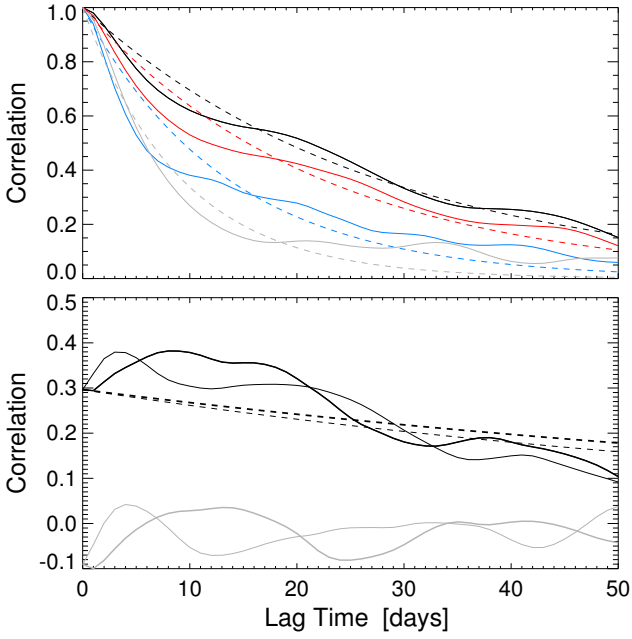

Figure 10. Top plot shows autocorrelation functions (solid) and exponential fits (dashed) based on 50 years of NCEP data. Autocorrelation functions $r(\mathbf{y}_L,\mathbf{y}_L;l)$ (black), $r(\mathbf{y}_T,\mathbf{y}_T;l)$ (red) and $r(\mathbf{y}_{p_s},\mathbf{y}_{p_s};l)$ (blue) are shown for January 1 at 150 hPa; for comparison the ACF $r(\mathbf{y}_L,\mathbf{y}_L;l)$ at 150 hPa is also shown for July 1 (grey). Bottom plot shows cross correlation functions $r(\mathbf{y}_T,\mathbf{y}_{p_s};l)$ (heavy curve) and $r(\mathbf{y}_{p_s},\mathbf{y}_T;l)$ (light curve) on January 1 (black) and July 1 (grey), both at 150 hPa. Fits to the January 1 cross correlation functions are shown in the dashed lines. Fits to July 1 have very short decay timescales close to zero (not shown).

where $l_{\max} = 50$ days. Fig. 6a-c plot $\tau(\boldsymbol{y}_L, \boldsymbol{y}_L)$, $\tau(\boldsymbol{y}_T, \boldsymbol{y}_T)$ and $\tau(\boldsymbol{y}_{p_s}, \boldsymbol{y}_{p_s})$ estimated by this procedure. For attributing sources of timescales to different terms, consider decomposing f into two parts: $f = f_1 + f_2$. In this notation the autocorrelation function of f is

$$\begin{aligned} r(f,f;l) &= s_{11} r(f_1,f_1;l) + s_{12}[r(f_1,f_2;l) + r(f_2,f_1;l)] \\ &+ s_{22} r(f_2,f_2;l),\ l \geq 0. \end{aligned} \tag{A2}$$

where $s_{11} = \sigma^2(f_1)/\sigma^2(f)$, $s_{12} = \sqrt{\sigma^2(f_1)\sigma^2(f_2)}/\sigma^2(f)$, and $s_{22} = \sigma^2(f_2)/\sigma^2(f)$.

Eqn. (A2) relates the correlation functions of f to the correlation functions of f_1 and f_2 and their cross correlation. Suppose we assume again that all cross-correlations and autocorrelations decay approximately exponentially. Then the estimated timescale for the sum f is related nonlinearly to the estimated timescales for the autocorrelation functions of f_1 and f_2, and to the cross correlation functions of f_1 with f_2. This suggests as a consistency condition that there is an estimated timescale $\hat{\tau}(f,f)$ such that $\exp(-l/\hat{\tau}(f,f))$ is consistent with

$$\begin{aligned} E(l) &= s_{11} \exp[-l/\tau(f_1,f_1)] \\ &+ s_{12} r(f_1,f_2;0) \{\exp[-l/\tau(f_1,f_2)] + \exp[-l/\tau(f_2,f_1)]\} \\ &+ s_{22} \exp[-l/\tau(f_2,f_2)], \end{aligned} \tag{A3}$$

where all the terms in $E(l)$ are estimated according to (A1). We adopt a semianalytic procedure to determine an appropriate $\hat{\tau}$. Regarding $E(l)$ as a continuous function of the lag time l, we seek a timescale $\hat{\tau}$ that minimizes the cost function

$$\int_0^\infty dl\, [\exp(-l/\hat{\tau}) - E(l)]^2 .$$

This integral is a sum of exponentials, and from it a polynomial expression for $\hat{\tau}$ in terms of the variance coefficients s_{11}, etc., the timescales $\tau(f_1,f_1)$ etc., and the cross correlation at lag zero $r(f_1,f_2;0)$ is found. This expression is minimized with respect to $\hat{\tau}$, which results in another polynomial. The roots of this second polynomial are determined numerically. To attribute persistence to the effects of particular correlations, we set multiplicative coefficients to zero in these expressions.

For example, for Fig. 6d, we carry out these calculations with $f_1 = \boldsymbol{y}_T$, and $f_2 = \boldsymbol{y}_{p_s}$. For Fig. 6f, we set $r(\boldsymbol{y}_{p_s}, \boldsymbol{y}_T; 0) = 0$ in the polynomial expression, recalculate $\hat{\tau}$, and subtract the result from the original NAM timescale in Fig. 6a. To provide a sense of how close the correlation functions are to exponentials, we show NH correlation functions in Figure 10 based on 50 years of NCEP data. All curves shown are for 150 hPa. We choose this lower stratospheric pressure level as it is a region of strong stratosphere-troposphere coupling. Even based on 50 years of data, the ACFs shown in the top plot are not perfectly exponential. Nonetheless the estimated timescale $\hat{\tau}$ is a reasonably good approximation, as seen in Figs. 6a, d, and e. The two cross correlation functions are compared during stratospherically active and inactive seasons in the bottom panel of Fig. 10. Note that while the cross correlation time scales increase during the stratospherically active season similar to the ACF timescales, they are indistinguishable from zero during stratospherically inactive seasons. Furthermore, while their correlation peaks during mid winter at about 0.3, it has a very slow decay time, and as noted in Section 3.2 serves to enhance persistence during the active seasons.

Acknowledgments. The authors would like to thank three anonymous reviewers for comments which helped to improve the manuscript We acknowledge E .P. Gerber for the use of code and the support of the Canadian Foundation for Climate and Atmospheric Science (grant GR-506) and the Natural Science and Engineering Research Council of Canada.

References

Baldwin, M. P., and T. J. Dunkerton (1999), Propagation of the Arctic Oscillation from the Stratosphere to the Troposphere, *J. Geophys. Res.*, *104*, 30937–30946, doi:10.1029/1999JD900445.

Baldwin, M. P., and T. J. Dunkerton (2001), Stratospheric Harbingers of Anomalous Weather Regimes, *Science*, *294*, 581–584, doi:10.1126/science.1063315.

Baldwin, M. P., and D. W. J. Thompson (2009), A critical comparison of stratosphere-troposphere coupling indices, *QJRMS*, *135*, 1661–1672, doi:10.1002/qj.479.

Baldwin, M. P., D. B. Stephenson, D. W. J. Thompson, T. J. Dunkerton, A. J. Charlton, and A. O'Neill (2003), Stratospheric Memory and Skill of Extended-Range Weather Forecasts, *Science*, *301*, 636–640, doi:10.1126/science.1087143.

Cai, M., and R.-C. Ren (2007), Meridional and downward propagation of atmospheric circulation anomalies. Part I: Northern hemisphere cold season variability., *J. Atmos. Sci.*, *64*, 1880–1901, doi:10.1175/JAS3922.1.

Chan, C. J. and R. A. Plumb (2009), The response to stratospheric forcing and its dependence on the state of the troposphere, *J. Atmos. Sci.*, *66*, 2107–2115, doi:10.1175/2009JAS2937.1.

Charlton-Perez, A. J., and A. O'Neill (2010), On the Sensitivity of Annular Mode Dynamics to Stratospheric Radiative Time Scales, *J. Climate*, *23*, 476–+, doi:10.1175/2009JCLI2995.1.

Gerber, E. P., and L. M. Polvani (2009), Stratosphere-Troposphere Coupling in a Relatively Simple AGCM: The Importance of Stratospheric Variability, *J. Climate*, *22*, 1920–+, doi:10.1175/2008JCLI2548.1.

Gerber, E. P., L. M. Polvani, and D. Ancukiewicz (2008a), Annular mode time scales in the Intergovernmental Panel on Climate Change Fourth Assessment Report models, *Geophys. Res. Lett.*, *35*, L22707, doi:10.1029/2008GL035712.

Gerber, E. P., S. Voronin, and L. M. Polvani (2008b), Testing the Annular Mode Autocorrelation Time Scale in Simple Atmospheric General Circulation Models, *Mon. Wea. Rev.*, *136*, 1523–+, doi:10.1175/2007MWR2211.1.

Gerber, E. P., M. P. Baldwin, and L. M. Polvani (2010), Stratosphere-Troposphere Coupling and Annular Mode Variability in Chemistry-Climate Models, *J. Geophys. Res.*, *115*, D00M06, doi:10.1029/2009JD013770.

Holton, J. R., and C. Mass (1976), Stratospheric vacillation cycles, *J. Atmos. Sci.*, *33*, 2218–2225, doi:10.1175/1520-0469(1976)033⟨2218%3ASVC⟩2.0.CO%3B2.

Hu, Y., and K. K. Tung (2002), Interannual and decadal variations of planetary-wave activity, stratospheric cooling, and Northern Hemisphere annular mode, *J. Climate*, *15*, 1659–1673 doi:10.1175/1520-0442(2002)015⟨1659%3AIADVOP⟩2.0.CO%3B2.

Kalnay, E., et al. (1996), The NCEP/NCAR 40-Year Reanalysis Project., *Bull. Amer. Met. Soc.*, *77*, 437–472, doi:10.1175/1520-0477(1996)077⟨0437:TNYRP⟩2.0.CO;2.

Keeley, S. P. E., and R. T. Sutton (2009), Does the North Atlantic Oscillation show unusual persistence on intraseasonal timescales?, *Geophys. Res. Lett.*, *36*, 22706, doi:10.1029/2009GL040367.

Kidston, J., and E. P. Gerber (2010), Intermodel variability of the poleward shift of the austral jet stream in the CMIP3 integrations linked to biases in 20th century climatology, *Geophys. Res. Lett.*, *37*, L09708, doi:10.1029/2010GL042873.

Kushner, P. J. (2010), Annular Modes of the Troposphere and Stratosphere, in *The Stratosphere: Dynamics, Transport and Chemistry.*, vol. 190, edited by Polvani, L. M., Sobel, A. H. & Waugh, D. W., AGU, Washington, D. C.

Limpasuvan, V., and D. L. Hartmann (2000), Wave-maintained annular modes of climate variability., *J. Climate*, *13*, 4414–4429, doi:10.1175/1520-0442(2000)013⟨4414%3AWMAMOC⟩2.0.CO%3B2.

Limpasuvan, V., D. L. Hartmann, D. W. J. Thompson, K. Jeev, and Y. L. Yung (2005), Stratosphere-troposphere evolution during polar vortex intensification, *J. Geophys. Res.*, *110*, D24101, doi:10.1029/2005JD006302.

Lorenz, D. J., and D. L. Hartmann (2001), Eddy-Zonal Flow Feedback in the Southern Hemisphere., *J. Atmos. Sci.*, *58*, 3312–3327, doi:10.1175/1520-0469(2001)058⟨3312:EZFFIT⟩2.0.CO;2.

Lorenz, D. J., and D. L. Hartmann (2003), Eddy-Zonal Flow Feedback in the Northern Hemisphere Winter., *J. Climate*, *16*, 1212–1227, doi:10.1175/1520-0442(2003)16⟨1212:EFFITN⟩2.0.CO;2.

McDaniel, B. A., and R. X. Black (2005), Intraseasonal dynamical evolution of the Northern Annular Mode., *J. Climate*, *18*, 3820–3839, doi:10.1175/JCLI3467.1.

Newman, P. A., E. R. Nash, and J. E. Rosenfield (2001), What controls the temperature of the Arctic stratosphere during the spring?, *J. Geophys. Res.*, *106*, 19999–20010, doi:10.1029/2000JD000061.

Polvani, L. M., and D. W. Waugh (2004), Upward wave activity flux as precursor to extreme stratospheric events and subsequent anomalous surface weather regimes, *J. Climate*, *17*, 3548–3554, doi:10.1175/1520-0442(2004)017⟨3548%3AUWAFAA⟩2.0.CO%3B2.

Robinson, W. A. (2000), A baroclinic mechanism for the eddy feedback on the zonal index., *J. Atmos. Sci.*, *57*, 415–422, doi:10.1175/1520-0469(2000)057⟨0415%3AABMFTE⟩2.0.CO%3B2.

Scinocca, J. F., N. A. McFarlane, M. Lazare, J. Li, and D. Plummer (2008), The cccma third generation agcm and its extension into the middle atmosphere, *Atmos. Chem. and Phys. Discuss.*, *8*, 7883–7930, doi:10.5194/acpd-8-7883-2008.

Shaw, T. A., and J. Perlwitz (2010), The Impact of Stratospheric Model Configuration on Planetary-Scale Waves in Northern Hemisphere Winter, *J. Climate*, *23*, 3369–3389, doi:10.1175/2010JCLI3438.1.

Shaw, T. A., M. Sigmond, and T. G. Shepherd (2009), Sensitivity of simulated climate to conservation of momentum in gravity wave drag parameterization, *J. Climate*, *22*, 2726–2742, doi:10.1175/2009JCLI2688.1.

Siegmund, P. (2005), Stratospheric Polar Cap Mean Height and Temperature as Extended-Range Weather Predictors, *Mon. Wea. Rev.*, *133*, 2436-2448, doi:10.1175/MWR2985.1.

Sigmond, M., and J. F. Scinocca (2010), The influence of the basic state on the northern hemisphere circulation response to climate change, *J. Climate*, *23*, 1434–1446, doi:10.1175/2009JCLI3167.1.

Sigmond, M., J. F. Scinocca, and P. J. Kushner (2008), Impact of the Stratosphere on Tropospheric Climate Change, *Geophys. Res. Lett.*, *35*, L12706, doi:10.1029/2008GL033573.

Song, Y., and W. A. Robinson (2004), Dynamical Mechanisms for Stratospheric Influences on the Troposphere., *J. Atmos. Sci*, *61*, 1711–1725, doi:10.1175/1520-0469(2004)061⟨1711:DMFSIO⟩2.0.CO;2.

Thompson, D. W. J., and J. M. Wallace (1998), The Arctic Oscillation signature in the wintertime geopotential height and temperature fields, *Geophys. Res. Lett.*, *25*, 1297–1300, doi:10.1029/98GL00950.

Thompson, D. W. J., and J. M. Wallace (2000), Annular Modes in the Extratropical Circulation. Part I: Month-to-Month Variability., *J. Climate*, *13*, 1000–1016, doi:10.1175/1520-0442(2000)013⟨1000%3AAMITEC⟩2.0.CO%3B2.

Thompson, D. W. J., J. C. Furtado, and T. G. Shepherd (2006), On the tropospheric response to anomalous stratospheric wave drag and radiative heating, *J. Atmos. Sci.*, *63*, 2616–2629, doi:10.1175/JAS3771.1.

Uppala, S. M., et al. (2005), The ERA-40 re-analysis, *QJRMS*, *131*, 2961–3012, doi:10.1256/qj.04.176.

Vallis, G. K., E. P. Gerber, P. J. Kushner, and B. A. Cash (2004), A mechanism and simple dynamical model of the North Atlantic Oscillation and annular modes., *J. Atmos. Sci.*, *61*, 264–280, doi:10.1175/1520-0469(2004)061⟨0264%3AAMASDM⟩2.0.CO%3B2.

Paul J. Kushner and L. R. Mudryk, Department of Physics, University of Toronto, 60 St. George Street, Toronto, Ontario, Canada, M5S 1A7. (paul.kushner@utoronto.ca; mudryk@atmosp.physics.utoronto.ca